ACS OMEGA

Open Access

http://pubs.acs.org/journal/acsodf

Article

Chemical States of Stainless Steel in nm to Several Tens of nm Region from Surface Observed by the Depth-Resolved X-ray Absorption Spectroscopy

Kenta Amemiya* and Kaoruho Sakata

Cite This: *ACS Omega* 2024, 9, 18593−18598

Read Online

ACCESS | Metrics & More | Article Recommendations

ABSTRACT: Chemical states of Fe, Cr, Ni, Mn, and O in stainless steel, SS304, are nondestructively observed over a wide range of depth from nanometer (nm) to several tens of nm by means of the depth-resolved X-ray absorption spectroscopy in the soft X-ray region. It is revealed that Cr is more oxidized in the surface region than the inner region, while Fe is also oxidized at the surface though the oxidation is less prominent compared to Cr. The chemical states of Cr are described by a mixture of Cr−O and Cr−OH coordinations, with more OH components at the surface. Mn and Ni spectra show MnO and metallic Ni features, respectively, throughout the depth of at least up to several tens of nm.

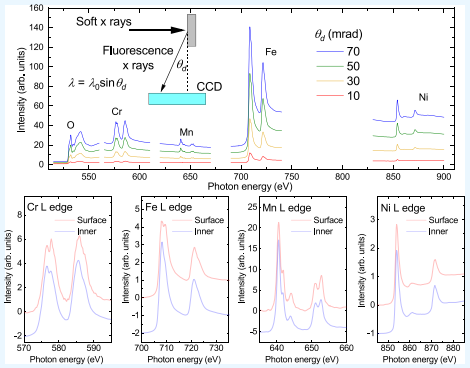

INTRODUCTION

The origin of the corrosion resistance of stainless steels (SSs) has been extensively studied for many decades.[1−22] It has been revealed that the surface of the SS is covered with a few nanometer (nm) thick oxides, which acts as a protection layer against further reaction into the inner region. For example, a recent study using X-ray absorption spectroscopy (XAS) combined with X-ray standing wave (XSW)[23,24] reported that a 2 nm thick passive surface layer consists of oxidized Fe and Cr.[14,16] Note that they did not observe the SS itself but used a 4 nm thick FeCrNi film with a metal composition close to that of SS304. This is because the XSW requires a multilayer substrate below the specimen in order to generate the standing wave, which is essential to achieve the depth-resolved analysis.[23,24]

Several experimental techniques have been applied to observe the structure and chemical states of SSs around the surface. Grazing-incidence X-ray diffraction (GIXRD) with different incidence angles has been used to determine the depth-resolved structural change around the surface, although information on the minor elements such as Cr and Ni cannot be obtained. The chemical components around the surface of SS have been studied using conventional XAS in the hard X-ray region, which is not sufficiently surface sensitive. It should be noted here that some attempts have been made to develop surface-sensitive XAS techniques in the hard X-ray region, by adopting the grazing-incidence conditions including the (total) reflection mode measurements.[25−28] Although these techniques achieved nanometer-order surface sensitivity, one must be careful in the depth-dependent analysis because the penetration depth of incident X-rays strongly depends on the X-ray photon energy especially around the absorption edge, at which the index of refraction drastically changes. X-ray photoemission spectroscopy (XPS) is a surface-sensitive technique, which can determine the chemical states of each element, but sometimes the technique is too surface sensitive, with typical probing depth of several nanometers, even if the hard X-rays are used.

Recently, a depth-resolved XAS technique in the soft X-ray region has been developed, which has nm scale depth resolution.[29−31] In the technique, the probing depths are controlled by the detection angles of the fluorescence X-rays emitted after the X-ray absorption, and the probing depth ranges from less than 1 nm to several tens of nm. Note here that the probing depth, λ, does not mean that only the signal from the depth λ is detected, but that the signal attenuates by a factor of $1/e$ while passing through the thickness of λ.[30] One can obtain the depth profile of the chemical state by analyzing a set of XAS data at different probing depths. It is also noteworthy that almost all of the elements contained in SSs

Received: February 7, 2024
Revised: March 23, 2024
Accepted: March 28, 2024
Published: April 8, 2024

can be analyzed by using XAS in the soft X-ray region. In the present study, the chemical states of Fe, Cr, Ni, Mn, and O are revealed over a wide range of depth from nanometers to several tens of nanometers, by using the depth-resolved XAS in the soft X-ray region.

EXPERIMENTAL SECTION

The depth-resolved XAS experiments were conducted at a soft X-ray beamline, BL-16A, of the Photon Factory at High Energy Accelerator Research Organization, Japan.[32] A 0.1 mm thick SS304 sheet (Nilaco Corp.) with an approximate nominal composition of $Fe_{73}Cr_{17}Ni_7Mn_2Si_1$ was investigated after exposure to air for more than 10 years in the room for the synchrotron radiation experiments at the Photon Factory, with typical temperature and humidity of 300 K and 25%, respectively. The setup for the measurement is schematically illustrated in Figure 1. The sample was placed with its surface

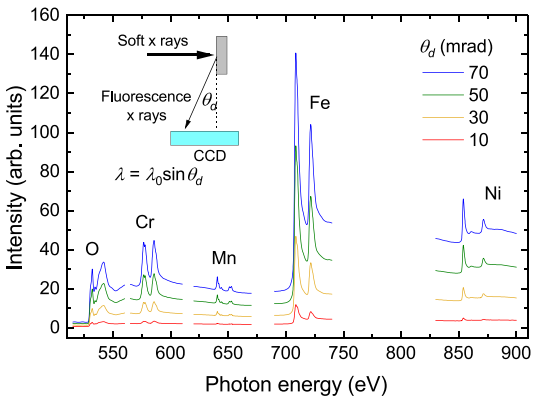

Figure 1. XAS data taken at different detection angles, θ_d, together with a concept for the depth-resolved XAS technique.

facing the incident soft X-rays in the normal incidence configuration. The fluorescence X-rays emitted at the relaxation process after the absorption of the incident soft X-rays were collected by a soft X-ray CCD camera (BITRAN, BL-501X) with a pixel size of 13 × 13 μm^2, placed below the sample. Thus, a set of XMCD data with different detection angles of the fluorescence X-rays, corresponding to different probing depths, were recorded at once.[31] In the present experiment, the detection angles θ_d ranged from 2.5 to 90 mrad from the surface plane. The probing depth, λ, is estimated by $\lambda = \lambda_0 \sin\theta_d$, where λ_0 is the attenuation length of the fluorescence X-ray.

RESULTS AND DISCUSSION

X-ray absorption spectra for all measured elements are summarized in Figure 1 for representative detection angles, θ_d. Since the spectra are shown without normalization, the signal intensity reflects the content of each element as well as the probability for the fluorescence X-ray emission and the detection efficiency of the CCD camera. In addition, the XAS signal increases with increasing θ_d, due to the increase in the contribution from a deeper part of the sample. To investigate the depth dependence of the element compositions, the Cr and Fe L-edge XAS data at two different θ_d values are shown in Figure 2. First, let us focus on the edge-jump intensity, which is the difference between the absorption intensities at the lower and higher X-ray energy regions of the adsorption edge. Note

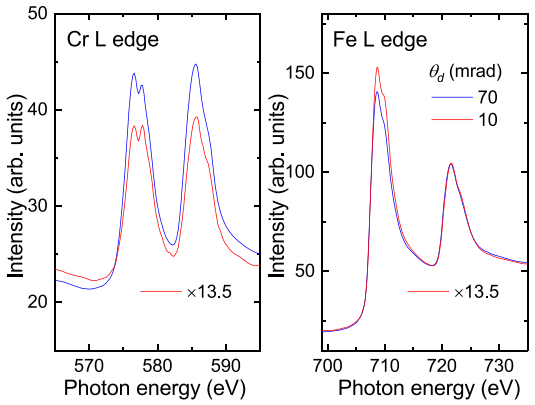

Figure 2. Cr and Fe L-edge XAS data for detection angles, θ_d, of 10 and 70 mrad. The spectra for θ_d = 10 mrad are multiplied by a factor of 13.5.

that the edge-jump intensity does not depend on the chemical states, but solely on the amount of the element. On the other hand, the XAS peak shape reflects the chemical states, which will be discussed later. Here, the data for θ_d = 10 mrad are multiplied by a factor of 13.5, in order to match the edge-jump intensities between θ_d = 10 and 70 mrad at the Fe L edge. The edge-jump intensities at the Cr L edge do not match, however, which indicates that the Fe/Cr ratio is not uniform in depth. The edge-jump intensity at the Cr L edge for θ_d = 10 mrad is smaller than that for θ_d = 70 mrad after being multiplied by 13.5, which suggests that the Cr/Fe composition ratio is smaller around the surface. The Cr/Fe edge-jump ratio is plotted as a function of θ_d in Figure 3.

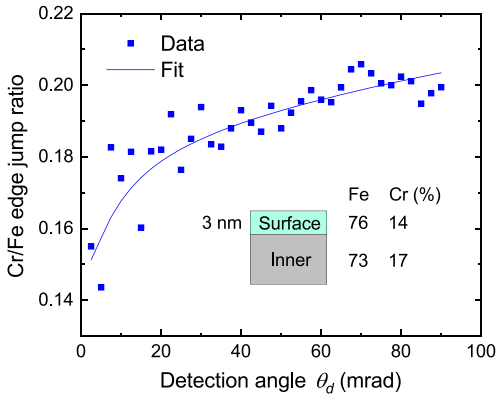

Figure 3. Detection angle, θ_d, dependence of the edge-jump ratio between Cr and Fe L-edge XAS (dot). Fitting result (line) is shown together with the estimated Fe and Cr compositions in the surface and inner regions.

To estimate the depth dependence of the Cr/Fe composition ratio, we fitted the edge-jump ratio assuming a simple model as shown in the figure. The sample is divided into surface and inner regions, and the thickness of the surface region is assumed to be t_{surf}. The edge-jump intensity, I_M^{edge}, where M corresponds to Cr or Fe, is expressed by

$$I_M^{edge}(\lambda_M) = c_M(\lambda_M) I_0(E_M) \int_0^\infty a_M(z) \exp\left(-\frac{z}{\lambda_M}\right) \exp\left(-\frac{1}{\cos\theta} \int_0^z \mu(E_M, z')dz'\right) dz \quad (1)$$

https://doi.org/10.1021/acsomega.4c01226
ACS Omega 2024, 9, 18593−18598

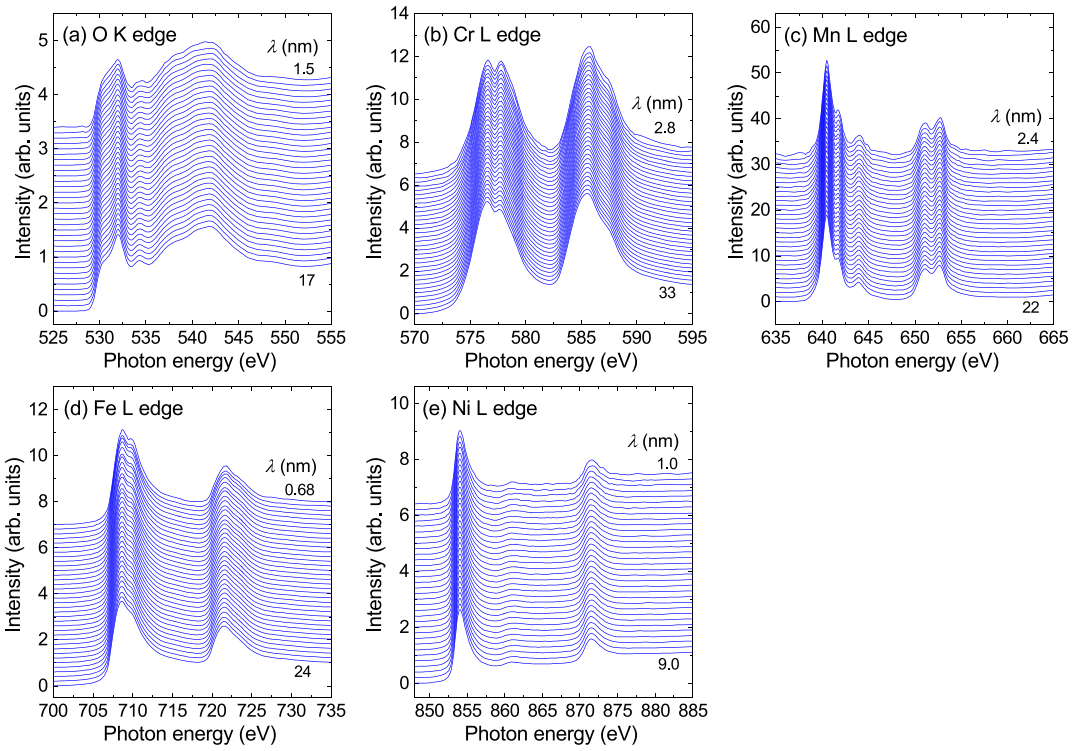

Figure 4. (a) O K-, (b) Cr L-, (c) Mn L-, (d) Fe L-, and (e) Ni L-edge XAS data taken at different probing depths, λ. Each spectrum is normalized to the edge jump.

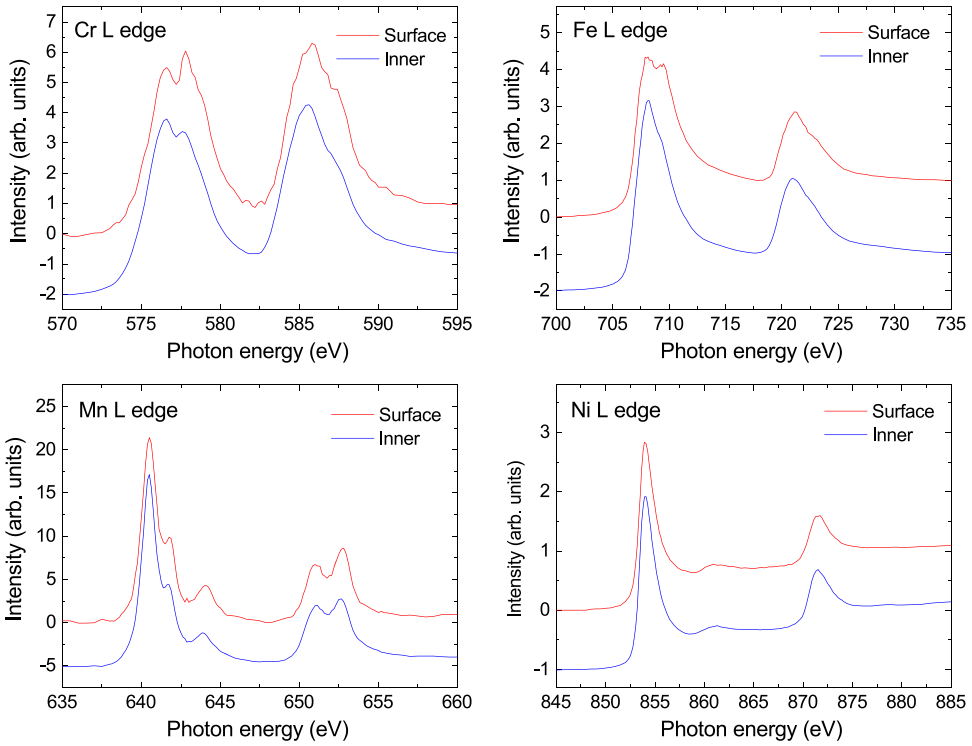

Figure 5. Extracted XAS data for the surface and inner regions.

where λ_M, E_M, I_0, a_M, z, and μ denote the escape depth of the fluorescence X-ray for M, photon energy at the M L edge, intensity of incident X-ray, composition of M, depth from the surface, and absorption coefficient, respectively, while c is a constant including the emission and detection efficiencies for the fluorescence X-rays. θ is the X-ray incidence angle from the surface normal, which was zero in the present experiments. According to the above-mentioned model, a_M is different between the surface and inner regions, so the integral is separately performed for $z = 0 - t_{surf}$ and $z = t_{surf} - \infty$. Here, the Cr and Fe compositions in the inner region are fixed at the bulk values, 17 and 73%, respectively, and those in the surface

https://doi.org/10.1021/acsomega.4c01226
ACS Omega 2024, 9, 18593−18598

region are set as fitting parameters. The optimized parameters and fitted curve are shown in Figure 3. The result shows that the Cr composition is slightly smaller at the surface, which can contradict the common understanding, in which Cr is believed to gather at the surface to make the passivation layer. This discrepancy might originate from the relatively small probing depth, up to several tens of nanometers, in the present experiment. Although we assumed that the Cr/Fe ratio in the inner region below t_{surf} is the same as the bulk value, the Cr/Fe ratio in the region might be still larger than the bulk value, and we would observe the slight change at the very surface region. Note that we can not determine the absolute composition but observe the relative change depending on the depth only around the surface.

To investigate the depth-dependent changes in chemical states for each element, XAS data at different probing depths, λ, are shown in Figure 4. Here, all spectra are normalized to the edge-jump intensity. The O K-, Cr L-, and Fe L-edge XAS show significant probing depth dependence, while the Mn and Ni L-edge XAS exhibit a similar spectrum independent of the probing depth. For instance, a peak at ∼578 eV in the Cr L-edge XAS, which is at the higher-energy side of the main peak, becomes more prominent at smaller probing depth, λ. Since the peak at ∼578 eV is attributed to Cr oxides or hydroxides, it is directly suggested that Cr at the surface of the sample is more oxidized compared to that in the inner region. A similar probing depth dependence is found in the Fe L-edge XAS, in which a peak at ∼710 eV becomes prominent at a smaller probing depth. Again, it is suggested that Fe at the surface of the sample is more oxidized. On the other hand, Mn and Ni L-edge XAS show little probing depth dependence, suggesting the same chemical state independent of depth. The Mn L-edge XAS shows characteristic features for MnO, while the Ni L-edge XAS is similar to that for metallic Ni.

From a series of XAS data at different probing depths, XAS for the surface and inner regions is extracted by assuming that the thickness of the surface region is 3 nm. The experimentally observed XAS signal at the probing depth, λ, is expressed by

$$I^{obs}(E, \lambda) = c(\lambda) I_0(E) \int_0^\infty \mu(E, z) \exp\left(-\frac{z}{\lambda}\right) \exp\left(-\frac{1}{\cos\theta} \int_0^z \mu(E, z')dz'\right) dz \quad (2)$$

where E denotes the photon energy, and I_0, z, μ, c, and θ are similarly defined as those in eq 1. The depth-dependent XAS, $\mu(E, z)$, is determined to reproduce a set of $I^{obs}(E, \lambda)$ at different probing depths, λ. The extracted XAS is shown in Figure 5. At the Cr L edge, the peak at ∼578 eV is prominent in the surface region, while it is small in the inner region, suggesting that Cr is oxidized mainly around the surface of the sample. The extracted XAS at the Fe L edge exhibits similar behavior, though the oxide peak at ∼710 eV is less prominent compared with that for Cr. In addition, the XAS in the inner region is almost the same as that for metallic Fe. Therefore, it is concluded that Cr is more oxidized than Fe around the surface of the sample. It is difficult to determine the Fe oxide species in the surface region because XAS for Fe_3O_4 and Fe_2O_3 are quite similar to each other.

On the other hand, the XAS at the Mn L edge is almost the same between the surface and inner regions, and the spectrum exhibits features for MnO. For the Ni L-edge XAS, the spectrum is also almost the same between the surface and inner regions, but it is characteristic of metallic Ni. Thus, it is indicated that MnO and metallic Ni uniformly exist through the depth of at least up to several tenths of nm, which is the probing depth of the present experiments.

To estimate the composition of the Cr oxides, the extracted spectra are compared with the standard spectra[33] for Cr_2O_3, $Cr(OH)_3$, and metallic Cr in Figure 6. Note here that it is

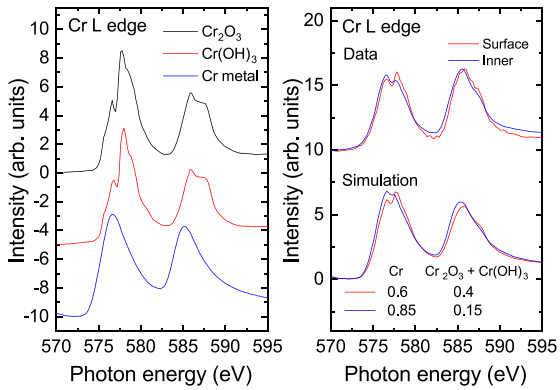

Figure 6. Standard spectra for Cr_2O_3, $Cr(OH)_3$ (reproduced from ref 33. Copyright 2017 Canadian Science Publishing.), and Cr metal at the Cr L edge (left) and extracted XAS data for the surface and inner regions, together with simulated spectra (right).

generally accepted that Cr around the surface of SS exists as an oxyhydroxide and oxide species together with adsorbed water. Therefore, it is expected that the observed XAS consists of some components characteristic of Cr−O and Cr−OH coordinations, which are roughly represented by the XAS spectra for Cr_2O_3 and $Cr(OH)_3$, respectively. The simulated XAS results using the standard spectra are also shown in Figure 6. Unfortunately, it is difficult to fit the data by using the standard spectra because the Cr L-edge XAS contains background signal originating from O K-edge absorption. Moreover, as mentioned above, the chemical state of Cr in SS is not simple, so that the fitting results does not directly reflect the chemical state, even if the spectra are quantitatively fitted. Therefore, we only discuss the qualitative changes in XAS depending on the components' standard spectra by showing the XAS simulation obtained by the linear combination of XAS for Cr and Cr_2O_3 or $Cr(OH)_3$ species with arbitrary compositions as indicated in Figure 6. Here, we do not distinguish Cr_2O_3 from $Cr(OH)_3$ because the Cr L-edge XAS data for these species are quite similar to each other. It is clearly suggested that Cr is more oxidized in the surface region.

Although the Cr L-edge XAS for Cr_2O_3 and $Cr(OH)_3$ are quite similar to each other as mentioned above, these species can be distinguished by using O K-edge XAS. To further investigate the oxidation state of Cr, O K-edge XAS for different probing depths are shown in Figure 7, together with the standard spectra[33,34] for Cr_2O_3, $Cr(OH)_3$, and Fe_3O_4. The observed O K-edge XAS has a prominent peak at ∼532 eV, which is attributed to Cr_2O_3. Interestingly, the intensity of the peak depends on the probing depth, and it is more prominent for a larger probing depth. Again, we do not fit the observed XAS because the O K-edge data must contain a lot of species other than Cr_2O_3, $Cr(OH)_3$, and Fe_3O_4, such as adsorbed water, Mn oxides, and surface contaminations. The simulation shows that the $Cr(OH)_3$ component increases at a smaller probing depth. It is thus suggested that there is more Cr−OH

https://doi.org/10.1021/acsomega.4c01226
ACS Omega 2024, 9, 18593−18598

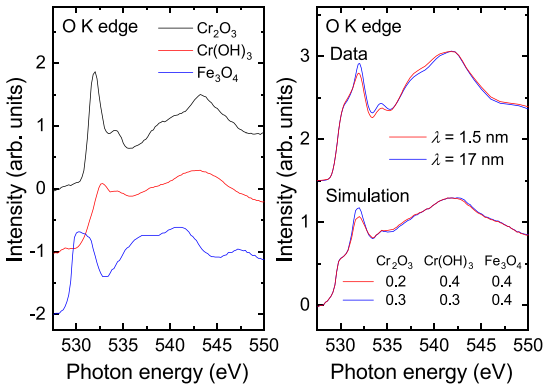

Figure 7. Standard spectra for Cr_2O_3, $Cr(OH)_3$ (reproduced from ref 33. Copyright 2017 Canadian Science Publishing), and Fe_3O_4 (reproduced from ref 34. Copyright 2005 AIP Publishing) at the O K edge (left), and XAS data for the probing depths, λ, of 1.5 and 17 nm, together with simulated spectra (right).

component at the surface of the sample compared to the inner region. This seems reasonable because air in the room contains water vapor.

CONCLUSIONS

Chemical states of Fe, Cr, Ni, Mn, and O in the SS304, were nondestructively investigated over a wide range of depth from nm to several tens of nm by means of depth-resolved XAS in the soft X-ray region. It was revealed that Cr is more oxidized in the ∼3 nm thick surface region. The chemical states of Cr were described by a mixture of Cr−O and Cr−OH coordinations, which are represented by Cr_2O_3 and $Cr(OH)_3$, respectively, with more OH coordination at the surface. Moreover, it was suggested that Fe is also oxidized in the surface region, though it is not as prominent as the Cr oxides, and that metallic Fe is dominant in the inner region. Mn and Ni spectra showed MnO and metallic Ni features, respectively, throughout the depth of at least up to several tens of nm. It has been demonstrated that the chemical states of almost all elements contained in SSs are observed in the near surface region without any special treatment of the specimen. The present technique is expected to be utilized to reveal the mechanism of the corrosion process of SSs under various conditions.

AUTHOR INFORMATION

Corresponding Author

Kenta Amemiya − *Institute of Materials Structure Science, High Energy Accelerator Research Organization, Tsukuba, Ibaraki 305-0801, Japan; Graduate Institute for Advanced Studies, SOKENDAI, Tsukuba, Ibaraki 305-0801, Japan;* orcid.org/0000-0003-2415-6686; Phone: +81 (0)29 879 6027; Email: kenta.amemiya@kek.jp; Fax: +81 (0)29 864 3202

Author

Kaoruho Sakata − *Institute of Materials Structure Science, High Energy Accelerator Research Organization, Tsukuba, Ibaraki 305-0801, Japan;* orcid.org/0000-0002-8470-0332

Complete contact information is available at: https://pubs.acs.org/10.1021/acsomega.4c01226

Notes

The authors declare no competing financial interest.

ACKNOWLEDGMENTS

The present work has been performed under the approval of the Photon Factory Program Advisory Committee (Nos. 2019S2-003 and 2022G553). The authors are grateful for the financial support of the JSPS KAKENHI Grant Nos. 19K22091, 21H04678, 22K19014, and 23K04700.

REFERENCES

(1) Saito, H.; Shibata, T.; Okamoto, G. The inhibitive action of bound water in the passive film of stainless steel against chloride corrosion. *Corros. Sci.* **1979**, *19*, 693−708.
(2) Kirchheim, R.; Heine, B.; Fischmeister, H.; Hofmann, S.; Knote, H.; Stolz, U. The passivity of iron-chromium alloys. *Corros. Sci.* **1989**, *29*, 899−917.
(3) Williams, D. E.; Newman, R. C.; Song, Q.; Kelly, R. G. Passivity breakdown and pitting corrosion of binary alloys. *Nature* **1991**, *350*, 216−219.
(4) Ropo, M.; Kokko, K.; Airiskallio, E.; Punkkinen, M. P. J.; Hogmark, S.; Kollár, J.; Johansson, B.; Vitos, L. First-principles atomistic study of surfaces of Fe-rich Fe-Cr. *J. Phys.: Condens. Matter* **2011**, *23*, No. 265004.
(5) Örnek, C.; Leygraf, C.; Pan, J. Passive film characterisation of duplex stainless steel using scanning Kelvin probe force microscopy in combination with electrochemical measurements. *npj Mater. Degrad.* **2019**, *3*, 8.
(6) Krishnan, S.; Dumbre, J.; Bhatt, S.; Akinlabi, E.; Ramalingam, R. Effect of Crystallographic Orientation on the Pitting Corrosion Resistance of Laser Surface Melted AISI 304L Austenitic Stainless Steel. *Int. J. Mech. Mechatronics* **2003**, *7*, 650−653.
(7) Olsson, C. O. A.; Landolt, D. Passive films on stainless steels -chemistry, structure and growth. *Electrochim. Acta* **2003**, *48*, 1093−1104 Microscopic and Nanoscopic Aspects of Corrosion and Corrosion Protection..
(8) Putz, A.; Althuber, M.; Zelić, A.; Westin, E. M.; Willidal, T.; Enzinger, N. Methods for the measurement of ferrite content in multipass duplex stainless steel welds. *Welding in the World* **2019**, *63*, 1075−1086.
(9) Venugopal, S.; Mannan, S.; Prasad, Y. Influence of strain rate and state-of-stress on the formation of ferrite in stainless steel type AISI 304 during hot working. *Mater. Lett.* **1996**, *26*, 161−165.
(10) Mayr, P.; Palmer, T.; Elmer, J.; Specht, E.; Allen, S. Formation of Delta Ferrite in 9 Wt Pct Cr Steel Investigated by In-Situ X-Ray Diffraction Using Synchrotron Radiation. *Metall. Mater. Trans. A* **2010**, *41*, 2462−2465.
(11) Kocijan, A.; Jenko, M.; Donik, Č. Electrochemical and XPS studies of the passive film formed on stainless steels in borate buffer and chloride solutions. *Corros. Sci.* **2007**, *49*, 2083−2098.
(12) Jiang, R.; Wang, Y.; Wen, X.; Chen, C.; Zhao, J. Effect of time on the characteristics of passive film formed on stainless steel. *Appl. Surf. Sci.* **2017**, *412*, 214−222.
(13) Maurice, V.; Marcus, P. Progress in corrosion science at atomic and nanometric scales. *Prog. Mater. Sci.* **2018**, *95*, 132−171.
(14) Garai, D.; Solokha, V.; Wilson, A.; Carlomagno, I.; Gupta, A.; Gupta, M.; Reddy, V. R.; Meneghini, C.; Carla, F.; Morawe, C.; Zegenhagen, J. Studying the onset of galvanic steel corrosion in situ using thin films: film preparation, characterization and application to pitting. *J. Phys.: Condens. Matter* **2021**, *33*, 125001.
(15) Frankel, G. S. Pitting Corrosion of Metals: A Review of the Critical Factors. *J. Electrochem. Soc.* **1998**, *145*, 2186.
(16) Garai, D.; Carlomagno, I.; Solokha, V.; Wilson, A.; Meneghini, C.; Morawe, C.; Murzin, V.; Gupta, A.; Zegenhagen, J. Swelling of Steel Film by Hydrogen Absorption at Cathodic Potential in Electrolyte. *phys. status solidi b* **2020**, *257*, No. 2070027.
(17) Briant, C. L.; Mulford, R. A. Surface segregation in austenitic stainless steel. *Metall. Trans. A* **1982**, *13*, 745−752.

(18) Gui, Y.; Zheng, Z.; Gao, Y. The bi-layer structure and the higher compactness of a passive film on nanocrystalline 304 stainless steel. *Thin Solid Films* **2016**, *599*, 64−71.
(19) Ma, L.; Wiame, F.; Maurice, V.; Marcus, P. Origin of nanoscale heterogeneity in the surface oxide film protecting stainless steel against corrosion. *npj Mater. Degrad.* **2019**, *3*, 29.
(20) Ferreira, E. A.; Noce, R. D.; Fugivara, C. S.; Benedetti, A. V. Evaluation of 316L Stainless Steel Corrosion Resistance in Solution Simulating the Acid Hydrolysis of Biomass. *J. Electrochem. Soc.* **2011**, *158*, C95.
(21) Kumar, B. R.; Singh, R.; Mahato, B.; De, P.; Bandyopadhyay, N.; Bhattacharya, D. Effect of texture on corrosion behavior of AISI 304L stainless steel. *Mater. Charact.* **2005**, *54*, 141−147.
(22) Garai, D.; Wilson, A.; Carlomagno, I.; Meneghini, C.; Carla, F.; Hussain, H.; Gupta, A.; Zegenhagen, J. Structure of the Surface Region of Stainless Steel: Bulk and Thin Films. *phys. status solidi b* **2022**, *259*, No. 2100513.
(23) Zegenhagen, J. X-ray standing waves technique: Fourier imaging active sites. *Jpn. J. Appl. Phys.* **2019**, *58*, 110502.
(24) Zegenhagen, J. Surface structure determination with X-ray standing waves. *Surf. Sci. Rep.* **1993**, *18*, 202−271.
(25) Martens, G.; Rabe, P. The anomalous dispersion of the refractive index and the extended X-ray absorption fine structure at the K edge of Cu. *J. Phys. C: Solid State Physics* **1980**, *13*, L913.
(26) Heald, S. M. EXAFS at grazing incidence: Data collection and analysis. *Rev. Sci. Instrum.* **1992**, *63*, 873−878.
(27) Lützenkirchen-Hecht, D.; Frahm, R. Structural investigations of sputter deposited thin films: reflection mode EXAFS, specular and non specular X-ray scattering. *Physica B: Condens. Matter* **2000**, *283*, 108−113.
(28) Abe, H.; Nakayama, T.; Niwa, Y.; Nitani, H.; Kondoh, H.; Nomura, M. Observation of surface reduction of NiO to Ni by surface-sensitive total reflection X-ray spectroscopy using Kramers−Kronig relations. *Jpn. J. Appl. Phys.* **2016**, *55*, No. 062401.
(29) Amemiya, K.; Kitagawa, S.; Matsumura, D.; Abe, H.; Ohta, T.; Yokoyama, T. Direct observation of magnetic depth profiles of thin Fe films on Cu(100) and Ni/Cu(100) with the depth-resolved x-ray magnetic circular dichroism. *Appl. Phys. Lett.* **2004**, *84*, 936−938.
(30) Amemiya, K. Sub-nm resolution depth profiling of the chemical state and magnetic structure of thin films by a depth-resolved X-ray absorption spectroscopy technique. *Phys. Chem. Chem. Phys.* **2012**, *14*, 10477−10484.
(31) Sakamaki, M.; Amemiya, K. Nanometer-resolution depth-resolved measurement of florescence-yield soft x-ray absorption spectroscopy for FeCo thin film. *Rev. Sci. Instrum.* **2017**, *88*, No. 083901.
(32) Amemiya, K.; Toyoshima, A.; Kikuchi, T.; Kosuge, T.; Nigorikawa, K.; Sumii, R.; Ito, K. Commissioning of a Soft X-ray Beamline PF-BL-16A with a Variable-Included-Angle Varied-Line-Spacing Grating Monochromator. *AIP Conf. Proc.* **2010**, *1234*, 295−298.
(33) Wang, Z.; Alrehaily, L.; Joseph, J.; Wren, J.; Wang, J.; Sham, T. Scanning transmission X-ray microscopy studies of chromium hydroxide hollow spheres and nanoparticles formed by gamma-radiation. *Can. J. Chem.* **2017**, *95*, 1146.
(34) Yang, C. K.; Chiou, J. W.; Tsai, H. M.; Pao, C. W.; Jan, J. C.; Ray, S. C.; Yeh, C. L.; Huang, K. C.; Hsueh, H. C.; Pong, W. F.; Tsai, M. H.; Hsieh, H. H.; Lin, H. J.; Hou, T. Y.; Hsu, J. H. Electronic structure and magnetic properties of Al-doped Fe3O4 films studied by x-ray absorption and magnetic circular dichroism. *Appl. Phys. Lett.* **2005**, *86*, No. 062504.

https://doi.org/10.1021/acsomega.4c01226
ACS Omega 2024, 9, 18593−18598